(Received 23 December 2025, Accepted 15 January 2026, Scheduled 31 January 2026)

Sensorless Composite Control of Permanent Magnet Synchronous Motor Based on Fuzzy Adaptive EDS-PLL

Zhuang Qiu[1], Zhonggen Wang[1,*], and Wenyan Nie[2]

[1]School of Electrical and Information Engineering, Anhui University of Science and Technology, Huainan 232001, China
[2]School of Mechanical and Electrical Engineering, Huainan Normal University, Huainan 232001, China

ABSTRACT: To address the inherent chattering issue in traditional sliding mode observers for the sensorless control of permanent magnet synchronous motors, an improved strategy combining a Fuzzy Adaptive Higher-order Sliding Mode Observer (HAFSMO) and a composite logarithmic sliding mode locked loop (EDS-PLL) is proposed. First, a higher-order adaptive sliding mode observer is designed, in which an exponential saturation smoothing function (ESSF) replaces the traditional sign function, and fuzzy control is employed to dynamically adjust the boundary layer parameters, enabling a smooth estimation and convergence of the back electromotive force within a finite time. Second, in the phase-locked loop stage, the exponential saturation smoothing function is integrated with the composite logarithmic sliding mode control to construct a composite logarithmic sliding mode phase-locked loop, further enhancing the accuracy of the rotor position observation. Finally, a simulation model was built on the MATLAB/Simulink platform for verification. Both the simulated and experimental results demonstrate that this method effectively suppresses system chattering and improves the accuracy of rotor position observation and overall system performance, thereby validating the effectiveness of the proposed sensorless control strategy.

1. INTRODUCTION

Permanent Magnet Synchronous Motors (PMSMs) are widely applied in new energy vehicles [1], rail transportation [2], aerospace [3], and industrial automation [4] because of their high-power density, high efficiency, excellent dynamic performance, and speed regulation characteristics. To achieve high-performance vector control of PMSMs, conventional methods typically rely on mechanical position sensors such as encoders or resolvers to acquire real-time rotor position information. However, the introduction of such sensors not only increases the system cost and size, but also reduces the overall reliability. Furthermore, these sensors present multiple challenges, including installation, maintenance, and noise immunity under harsh operating conditions [5]. Consequently, sensorless control technology has become a significant research direction in PMSM drive systems.

Currently, sensorless control strategies for PMSMs are primarily divided into two categories: methods based on high-frequency signal injection, which are suitable for zero- or very low-speed operation [6], and methods based on the fundamental mathematical model of the motor, which are predominantly used for medium-to-high-speed applications. The core of the latter approach involves extracting rotor position and speed information by observing the back electromotive force (EMF) [7]. These methods include the Sliding Mode Observer (SMO) [8], Model Reference Adaptive System (MRAS) [9], and Extended Kalman Filter (EKF) [10] methods. Among them, SMO has been widely adopted for sensorless control of PMSMs owing to its simple structure and strong robustness against parameter variations and external disturbances [11]. However, traditional SMOs typically employ a discontinuous sign function as the switching term, which leads to significant high-frequency chattering in the estimated back EMF. This severely compromises the accuracy of the rotor position and speed estimation and degrades system stability [12].

To address these issues, several improved schemes have been proposed. For instance, Ref. [13] replaces the traditional switching term with an S-shaped function, improving the position estimation accuracy to some extent; however, its immunity to load disturbances remains limited. Ref. [14] introduces adaptive gains to construct an improved adaptive super-twisting sliding-mode observer, enhancing system stability, albeit at the cost of increased computational complexity, which affects real-time performance. Ref. [15] designs a higher-order terminal sliding mode observer using adaptive gains, effectively suppressing chattering and reducing back-EMF estimation errors; however, its capability to compensate for nonlinear disturbances remains insufficient. Ref. [16] substitutes the sign function with a hyperbolic tangent function, effectively reducing chattering and improving position estimation performance; however, the effectiveness of the method is sensitive to boundary layer parameters and sampling strategies. Ref. [17] proposes a composite nonlinear super-twisting sliding mode observer, mitigating chattering caused by switching control; however, there is still room for improvement in speed estimation accuracy. Ref. [18] designs a boundary layer adaptive fuzzy sliding mode observer, suppressing chattering via a sigmoid continuous function and employing fuzzy logic to adjust the boundary layer thickness online, combined with a phase locked loop (PLL) for rotor position extraction. However, conventional PLLs still exhibit shortcomings in terms of their estima-

* Corresponding author: Zhonggen Wang (zgwang@ahu.edu.cn).

tion accuracy and disturbance rejection capability. Ref. [19] compensates for phase lag by fusing SMO and PLL, improving estimation accuracy; however, the inherent estimation performance and disturbance rejection of traditional PLLs are limited. Ref. [20] combines an improved adaptive reaching law with a higher-order PLL structure, enhancing noise immunity and convergence speed; however, it leads to increased system complexity and difficulties in parameter tuning. In [21], a high-order logarithmic sliding mode observer is proposed by optimizing the sliding surface design and control law. Furthermore, an extended state observer based on a third-order super-twisting sliding mode algorithm is introduced into the phase-locked loop stage, which effectively suppresses speed chattering and significantly improves the estimation accuracy of both rotor position and rotational speed. In [22], an ESO is embedded within the PLL to replace the traditional proportional-integral (PI) regulator and adds a position compensation module, significantly improving the dynamic response and disturbance rejection of speed estimation. However, the performance of this method depends heavily on the accuracy of the front-end back-EMF observation.

Unlike methods that combine traditional sliding mode observers with phase-locked loops, this study proposes a novel strategy for the sensorless position control of permanent magnet synchronous motors, which integrates a fuzzy adaptive higher-order sliding mode observer with a composite logarithmic sliding mode phase-locked loop. The main contributions of this method are summarized as follows.

First, this paper integrates HAFSMO with EDS-PLL to construct a novel sensorless control architecture with robust disturbance rejection capability. At the observer level, the architecture employs fuzzy logic to adaptively adjust the boundary layer, significantly suppressing the inherent high-frequency chattering of traditional sliding mode control. At the phase-locked loop level, a composite logarithmic sliding surface is introduced, enhancing the dynamic accuracy and robustness of position tracking.

Second, compared with conventional SMO-PLL and existing improved schemes such as STASMO-NPLL, the proposed method demonstrates notable improvements in chattering suppression, dynamic response, and steady-state accuracy. Simulated and experimental results show that under various operating conditions, including no-load and sudden load changes, the proposed approach significantly reduces observation errors in speed and position, validating its superior dynamic and steady-state performance.

Finally, the strategy does not rely on high-precision position sensors. While enhancing system reliability and reducing hardware costs, it maintains high-precision control performance, making it suitable for high-dynamic applications such as new energy vehicles and industrial drives, with strong potential for engineering implementation.

2. MATHEMATICAL MODEL OF PMSM

To simplify the analysis, this study assumes that the three-phase windings of the permanent magnet synchronous motor are symmetrical, and core saturation, eddy current losses, and hysteresis losses are neglected. In the stationary reference frame (α-β), the stator voltage equation of the PMSM can be expressed as

$$\begin{bmatrix} u_\alpha \\ u_\beta \end{bmatrix} = \begin{bmatrix} R+pL_s & 0 \\ 0 & R+pL_s \end{bmatrix} \begin{bmatrix} i_\alpha \\ i_\beta \end{bmatrix} + \begin{bmatrix} e_\alpha \\ e_\beta \end{bmatrix} \quad (1)$$

In the equation, u_α and u_β, i_α and i_β, e_α and e_β represent the stator voltages, stator currents, and back electromotive forces on the α-β axes, respectively; R is the stator resistance; L_s is the stator inductance; and $p = \mathrm{d}/\mathrm{d}t$ is the differential operator.

According to Equation (1), the state equation of the stator current can be expressed as

$$\frac{\mathrm{d}}{\mathrm{d}t}\begin{bmatrix} i_\alpha \\ i_\beta \end{bmatrix} = -\frac{R}{L_s}\begin{bmatrix} i_\alpha \\ i_\beta \end{bmatrix} + \frac{1}{L_s}\begin{bmatrix} u_\alpha \\ u_\beta \end{bmatrix} - \frac{1}{L_s}\begin{bmatrix} e_\alpha \\ e_\beta \end{bmatrix} \quad (2)$$

where the back electromotive force can be expressed as:

$$\begin{bmatrix} e_\alpha \\ e_\beta \end{bmatrix} = \omega_e \psi_f \begin{bmatrix} -\sin\theta_e \\ \cos\theta_e \end{bmatrix} \quad (3)$$

where ω_e, ψ_f, and θ_e represent the electrical angular velocity, permanent magnet flux linkage, and electrical angle, respectively.

From Equation (3), it can be observed that the back electromotive force contains all the information regarding the rotor position and speed of the motor. Therefore, an accurate calculation of the rotor position and speed can only be achieved by accurately acquiring the back electromotive force.

3. DESIGN OF HAFSMO

3.1. Traditional Sliding Mode Observer

To obtain the estimated back electromotive force, the traditional sliding-mode observer is designed as:

$$\begin{aligned} \frac{\mathrm{d}}{\mathrm{d}t}\begin{bmatrix} \hat{i}_\alpha \\ \hat{i}_\beta \end{bmatrix} = & -\frac{R}{L_s}\begin{bmatrix} \hat{i}_\alpha \\ \hat{i}_\beta \end{bmatrix} + \frac{1}{L_s}\begin{bmatrix} u_\alpha \\ u_\beta \end{bmatrix} \\ & -\frac{1}{L_s}\begin{bmatrix} g*\mathrm{sign}(\tilde{i}_\alpha) \\ g*\mathrm{sign}(\tilde{i}_\beta) \end{bmatrix} \end{aligned} \quad (4)$$

In the equation, $\hat{i}_\alpha$ and $\hat{i}_\beta$ denote the estimated stator currents; $\tilde{i}_\alpha = \hat{i}_\alpha - i_\alpha$ and $\tilde{i}_\beta = \hat{i}_\beta - i_\beta$ denote the stator current estimation errors; u_α and u_β represent the control inputs of the observer; sign( ) is the switching function; and g is the sliding mode gain.

The sliding mode function is defined as:

$$\mathbf{s} = \begin{bmatrix} s_\alpha \\ s_\beta \end{bmatrix} = \begin{bmatrix} \tilde{i}_\alpha \\ \tilde{i}_\beta \end{bmatrix} = \begin{bmatrix} \tilde{i}_\alpha - i_\alpha \\ \tilde{i}_\beta - i_\beta \end{bmatrix} \quad (5)$$

By subtracting Equation (4) from Equation (2), the stator current error state equation can be expressed as

$$\frac{\mathrm{d}}{\mathrm{d}t}\begin{bmatrix} \tilde{i}_\alpha \\ \tilde{i}_\beta \end{bmatrix} = -\frac{R}{L_s}\begin{bmatrix} \tilde{i}_\alpha \\ \tilde{i}_\beta \end{bmatrix} + \frac{1}{L_s}\begin{bmatrix} e_\alpha \\ e_\beta \end{bmatrix} - \frac{1}{L_s}\begin{bmatrix} g*\mathrm{sign}(\tilde{i}_\alpha) \\ g*\mathrm{sign}(\tilde{i}_\beta) \end{bmatrix} \quad (6)$$

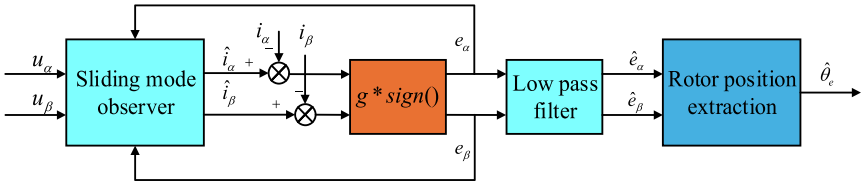

FIGURE 1. Block diagram of the traditional sliding mode observer.

From Equation (6), it can be seen that when the system state converges to the sliding surface ($\tilde{i}_\alpha = \tilde{i}_\beta = 0$), the back EMF can be expressed as

$$\begin{bmatrix} e_\alpha \\ e_\beta \end{bmatrix} = \begin{bmatrix} g * \text{sign}(\tilde{i}_\alpha) \\ g * \text{sign}(\tilde{i}_\beta) \end{bmatrix} \tag{7}$$

According to Equation (7), the use of a sign function leads to a discontinuous control law, causing high-frequency chattering in the back electromotive force estimation. This, in turn, affects the accuracy of the rotor position and speed observations, as well as the system stability. To address this issue, a low-pass filter must be introduced to suppress chattering.

$$\begin{cases} \frac{de_\alpha}{dt} = \frac{\left(-e_\alpha + g\text{sign}(\tilde{i}_\alpha)\right)}{\tau} \\ \frac{de_\beta}{dt} = \frac{\left(-e_\beta + g\text{sign}(\tilde{i}_\beta)\right)}{\tau} \end{cases} \tag{8}$$

The implementation principle of a traditional sliding mode observer is illustrated in Fig. 1.

3.2. HAFSMO

Conventional SMO based on the constant-rate reaching law suffers from issues such as a relatively slow system response and long convergence time. By contrast, higher-order sliding-mode observers offer faster dynamic responses and shorter convergence times. To this end, this study employed a higher-order super-twisting sliding-mode observer for the design. The fundamental form of the second-order super-twisting algorithm is as follows:

$$\begin{cases} \frac{d\hat{x}_1}{dt} = -k_1 \left|\bar{x}_1\right|^{0.5} \text{sign}(\bar{x}_1) + x_2 + \rho_1 \\ \frac{d\hat{x}_2}{dt} = -k_2 \text{sign}(\bar{x}_2) + \rho_2 \end{cases} \tag{9}$$

where x_i represents the estimated value of the state variable; $\bar{x}_i = \hat{x}_i - x_i$ denotes the observation error; k_i is the gain parameter of the observer; and ρ_i denotes the system disturbance.

Although second-order super-twisting sliding-mode observers effectively mitigate the chattering phenomenon inherent in traditional sliding-mode observers, they still exhibit certain limitations in terms of convergence speed and resistance to external disturbances. To address these shortcomings, this study proposes an adaptive higher-order super-twisting algorithm. By incorporating a nonlinear feedback mechanism, designing adaptive gains, adding compensatory terms, and increasing the system order, this algorithm significantly accelerates the convergence process and enhances disturbance rejection capabilities. Consequently, it has effectively improved the dynamic response and robustness of the system. The fundamental formulation is expressed as follows:

$$\begin{cases} \frac{dx_1}{dt} = -k_1 \left(\frac{2}{1+(|\bar{x}_1|+1)^{-z\bar{x}_1}}\right) \text{sign}(\bar{x}_1) - k_2\dot{\bar{x}}_1 \\ \qquad -k_3\bar{x}_1 + x_2 + \rho_1 \\ \frac{dx_2}{dt} = -k_4 \left(\frac{2}{1+(|\bar{x}_1|+1)^{-z\bar{x}_1}}\right) \text{sign}(\bar{x}_1) - k_5\dot{\bar{x}}_1 \\ \qquad +x_3 + \rho_2 \\ \frac{dx_3}{dt} = \eta\left[\tanh(k_6\bar{x}_1) + \tanh(k_7\dot{\bar{x}}_1)\right] + \rho_3 \\ \eta = k_{10}\frac{1+|\bar{x}_1|+|\dot{\bar{x}}_1|}{1+k_8|\bar{x}_1|^2+k_9\left|\dot{\bar{x}}_1\right|^2} \end{cases} \tag{10}$$

where k_i is the observer gain parameter ($k_i > 0$); z is a positive constant ($0 < z < 1$); η is the adaptive gain; and ρ_i is the system disturbance.

Owing to its dynamic adjustment capability, $-k_1(\frac{2}{1+(|\bar{x}_1|+1)^{-z\bar{x}_1}})\text{sign}(\bar{x}_1)$ can provide appropriate control gains under different states, thereby improving the convergence speed. The additional compensation term $-k_2\dot{\bar{x}}_1 - k_3\bar{x}_1$ enables the system to respond better to external disturbances, enhancing its anti-interference capability and stability. The adaptive gain η is used to dynamically adjust the gain of the control input x_3, allowing the system to adapt to different state magnitudes and optimize the convergence characteristics. When $|\bar{x}_1|$ decreases, η can still maintain a relatively large control gain, accelerating the convergence speed. When $|\bar{x}_1|$ increases, the nonlinear term in the denominator modulates the control gain, preventing excessive control action and improving stability.

Increasing the system order significantly enhances the finite-time convergence properties of the algorithm, achieving a faster dynamic response and higher steady-state accuracy. Simultaneously, the higher-order framework endows the system with an inherent ability to suppress bounded-rate disturbances, effectively improving the robustness in dynamically disturbed environments.

3.3. Exponential Saturation Smoothing Function-ESSF

A sign function was employed as the switching function in the higher-order sliding-mode observer described in the previous section. Although this function is simple to design and easy to implement, its discontinuity near the origin introduces significant high-frequency chattering. To effectively suppress this chattering, we designed an exponential saturation nonlinear

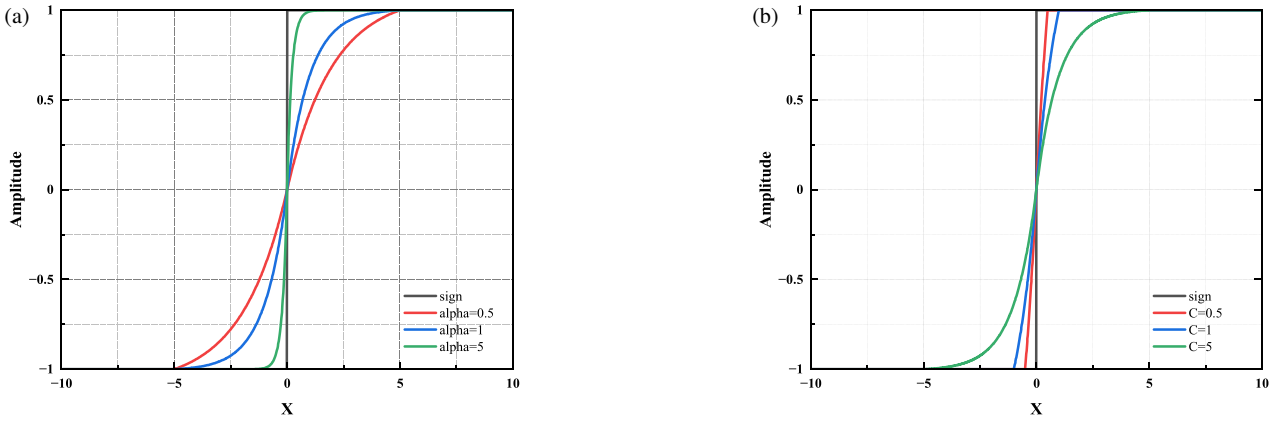

FIGURE 2. Switching functions under different parameter values. (a) Graph of $h(x)$ under different values of α. (b) Graph of $h(x)$ under different values of C.

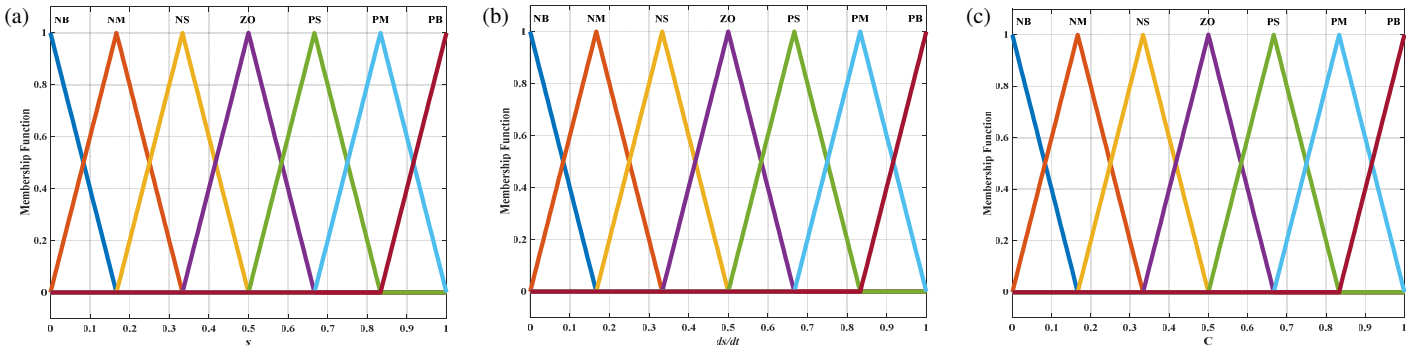

FIGURE 3. Membership function graphs of the input and output. (a) Membership function of input s; (b) Membership function of input ds/dt; (c) Membership function of output C.

transition function, expressed as follows:

$$h(x) = \begin{cases} 1 & x \geq C \\ \frac{1-e^{-\alpha x}}{1-e^{-\alpha C}} & 0 < x < C \\ -\frac{1-e^{-\alpha |x|}}{1-e^{-\alpha C}} & -C < x < 0 \\ -1 & x \leq -C \end{cases} \tag{11}$$

where α is a positive constant, and C represents the boundary layer.

In the equation, the selection of α and C is crucial during the design process, as it directly affects the chattering suppression effect and control precision of the system. The functions $h(x)$ corresponding to different values of α and C are shown in Fig. 2.

To further optimize system performance, fuzzy control was introduced in this study for adaptive parameter adjustment. Fuzzy control exhibits good adaptability to nonlinear systems and can dynamically adjust relevant parameters based on the real-time system state, thereby effectively matching the nonlinear characteristics of the system and enhancing overall stability. The designed fuzzy controller takes the error change rate as inputs, with the fuzzy linguistic sets for the input variables defined as {NB (Negative Big), NM (Negative Medium), NS (Negative Small), ZO (zero), PS (Positive Small), PM (Positive Medium), and PB (Positive Big)}. The fuzzy linguistic sets for the output variable are defined as {MM (minimum), S (small), MS (Medium Small), M (medium), MB (Medium Big), B (big), and Extra Large (EX)}. The membership functions for the inputs and outputs are shown in Fig. 3, and the control rules are listed in Table 1. The fuzzification process employed a triangular membership function, whereas defuzzification was performed using the centroid method. The sliding surface model adjusted via fuzzy control is illustrated in Fig. 4.

TABLE 1. Fuzzy control rules.

$S\backslash\dot{S}$	NB	NM	NS	ZO	PS	PM	PB
NB	PB	PB	PM	PM	PS	PS	PS
NM	PB	PM	PM	PS	PS	PS	PS
NS	PM	PM	PS	PS	PS	PS	PM
ZO	PM	PS	PS	ZO	PS	PS	PM
PS	PM	PS	PS	PS	PS	PM	PM
PM	PS	PS	PS	PS	PM	PM	PB
PB	PS	PS	PS	PM	PM	PB	PB

This fuzzy controller dynamically adjusts the boundary layer thickness C based on the magnitude of the error, with its de-

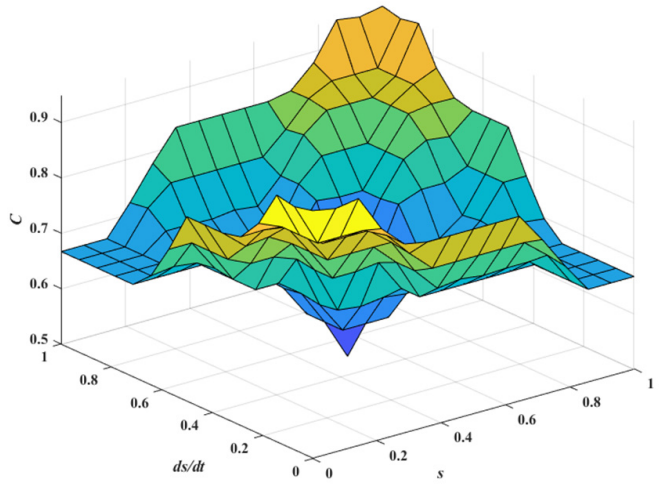

FIGURE 4. Input-output relationship.

sign logic outlined in Table 1. When the error is large, a larger C is set, at which point, the system operates far from the sliding surface. By combining a wider boundary layer with ESSF, high-frequency chattering can be effectively suppressed while maintaining stability, thereby preventing amplified chattering during startup or sudden load changes from compromising the accuracy of back-EMF observation. Despite the wider boundary layer, HAFSMO ensures rapid convergence without significantly degrading dynamic performance, thanks to its adaptive gain and nonlinear compensation mechanisms. When the error is small, a moderate or smaller C is output. In this state, the system approaches the sliding surface, and reducing the boundary layer helps improve control precision, enabling the observer to more accurately track variations in the back-EMF, thereby enhancing the accuracy of rotor position and speed estimation. This strategy essentially achieves a coordinated approach of "smoothing under large errors, precision under small errors." It not only strengthens the system's robustness during large dynamic processes but also ensures observation accuracy under small-signal conditions. Moreover, smooth switching is realized via ESSF, avoiding the hard-switching chattering associated with traditional sign functions.

In Fig. 4, the sliding surface function "s" is defined as the current estimation error, which characterizes the deviation between the observer output and the actual system state. "ds/dt" denotes the time derivative of the sliding surface function, i.e., the rate of change of the current estimation error, reflecting the dynamic behavior of the system state as it approaches the sliding surface. To further enhance the adaptability and regulation performance of the observer, the quantization ranges of both input variables s and ds/dt are set to [0, 1], and the quantization range of the output variable C is also set to [0, 1]. This range assignment is designed to ensure that the fuzzy rules exhibit good adaptability in practical systems, thereby effectively adjusting the dynamic response of the observer.

3.4. Performance Analysis

Based on Equations (4), (10), and (11), the mathematical model of HAFSMO is shown in Fig. 5.

$$\frac{\mathrm{d}}{\mathrm{d}t}\begin{bmatrix}\hat{i}_\alpha\\ \hat{i}_\beta\end{bmatrix}=-\frac{R}{L_s}\begin{bmatrix}\hat{i}_\alpha\\ \hat{i}_\beta\end{bmatrix}+\frac{1}{L_s}\begin{bmatrix}u_\alpha\\ u_\beta\end{bmatrix}-\frac{1}{L_s}\begin{bmatrix}k_1\left(\frac{2}{1+(|\bar{i}_\alpha|+1)^{-z\bar{i}_\alpha}}\right)h(\bar{i}_\alpha)+k_2\dot{\bar{i}}_\alpha+k_3\bar{i}_\alpha+Y_\alpha\\ k_1\left(\frac{2}{1+(|\bar{i}_\beta|+1)^{-z\bar{i}_\beta}}\right)h(\bar{i}_\beta)+k_2\dot{\bar{i}}_\beta+k_3\bar{i}_\beta+Y_\beta\end{bmatrix} \tag{12}$$

$$\begin{cases}Y_\alpha=\int\left(k_4\left(\frac{2}{1+(|\bar{i}_\alpha|+1)^{-z\bar{i}_\alpha}}\right)h(\bar{i}_\alpha)-k_5\dot{\bar{i}}_\alpha\right.\\ \left.+\int\left(k_{10}\frac{1+|\bar{i}_\alpha|+|\dot{\bar{i}}_\alpha|}{1+k_8|\bar{i}_\alpha|^2+k_9|\dot{\bar{i}}_\alpha|^2}\left[\tanh(k_6\bar{i}_\alpha)+\tanh(k_7\dot{\bar{i}}_\alpha)\right]\right)\right)\\ Y_\beta=\int\left(k_4\left(\frac{2}{1+(|\bar{i}_\beta|+1)^{-z\bar{i}_\beta}}\right)h(\bar{i}_\beta)-k_5\dot{\bar{i}}_\beta\right.\\ \left.+\int\left(k_{10}\frac{1+|\bar{i}_\beta|+|\dot{\bar{i}}_\beta|}{1+k_8|\bar{i}_\beta|^2+k_9|\dot{\bar{i}}_\beta|^2}\left[\tanh(k_6\bar{i}_\beta)+\tanh(k_7\dot{\bar{i}}_\beta)\right]\right)\right)\end{cases} \tag{13}$$

To validate the effectiveness of the designed HAFSMO, it is compared with the traditional sliding mode observer (SMO) and the super-twisting algorithm sliding mode observer (STASMO) [23] under a speed condition of 300 r/min. The estimated back electromotive force waveforms are shown in Fig. 6, where Fig. 6(a), Fig. 6(b), and Fig. 6(c) correspond to the results of SMO, STASMO, and HAFSMO, respectively. Fig. 7(a), Fig. 7(b), and Fig. 7(c) show the Fast Fourier Transform (FFT) analysis for the three methods. At the fundamental frequency of 58 Hz, the total harmonic distortion (THD) for SMO and STASMO was 48.75% and 26.76%, respectively, while the THD for HAFSMO was 25.85%. This represents reductions of 46.97% and 3.4% compared to the former two methods, respectively. These results indicate that the higher-order harmonics in the rotor flux are effectively suppressed owing to the inherent filtering characteristics of HAFSMO, thereby significantly improving the output waveform quality of the observer.

3.5. Stability Analysis

Define the Lyapunov function:

$$V=\frac{1}{2}\left(i_\alpha^2+i_\beta^2\right) \tag{14}$$

Take the derivative of V:

$$\dot{V}=i_\alpha\dot{i}_\alpha+i_\beta\dot{i}_\beta \tag{15}$$

Substituting Equation (10) yields:

$$\dot{V}=i_\alpha\left(-\frac{R}{L_S}i_\alpha+\frac{1}{L_S}u_\alpha-\frac{1}{L_S}\left[k_1\left(\frac{2}{1+(|\bar{i}_\alpha|+1)^{-z\bar{i}_\alpha}}\right)h(\bar{i}_\alpha)+k_2\dot{\bar{i}}_\alpha+k_3\bar{i}_\alpha+Y_\alpha\right]\right)+i_\beta\left(-\frac{R}{L_S}i_\beta+\frac{1}{L_S}u_\beta-\frac{1}{L_S}\left[k_1\left(\frac{2}{1+(|\bar{i}_\beta|+1)^{-z\bar{i}_\beta}}\right)h(\bar{i}_\beta)+k_2\dot{\bar{i}}_\beta+k_3\bar{i}_\beta\right.\right.$$

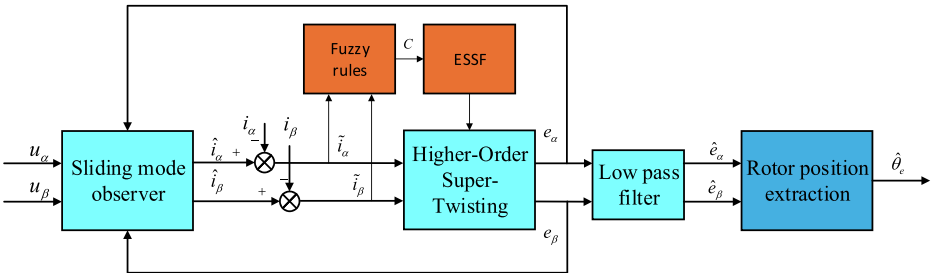

FIGURE 5. Block diagram of the HAFSMO.

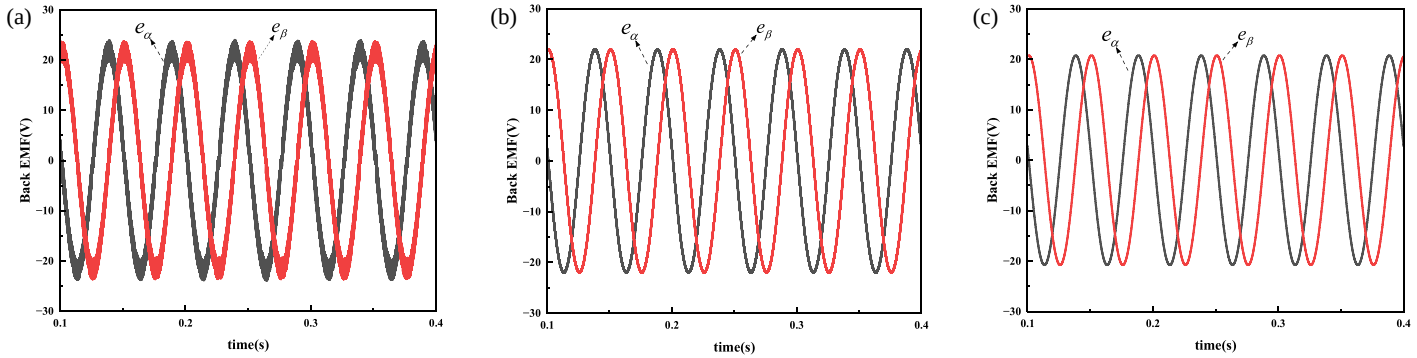

FIGURE 6. Estimated back electromotive force waveforms. (a) SMO; (b) STASMO; (c) HAFSMO.

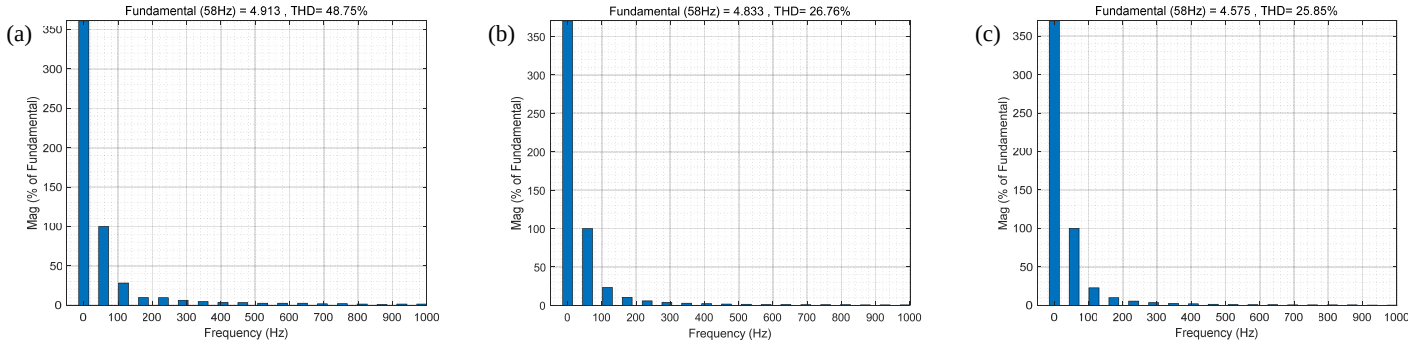

FIGURE 7. Back electromotive force harmonic analysis. (a) SMO; (b) STASMO; (c) HAFSMO.

$$+Y_\beta\Big]\Big) \tag{16}$$

Simplifying this gives:

$$\dot{V} = -\frac{R}{L_s}(i_\alpha^2 + i_\beta^2) + \frac{1}{L_s}(i_\alpha u_\alpha + i_\beta u_\beta) - \frac{1}{L_s}$$

$$\left\{\begin{pmatrix} i_\alpha\left[k_1\left(\frac{2}{1+(|\bar{i}_\alpha|+1)^{-z\bar{i}_\alpha}}\right)h(\bar{i}_\alpha) + k_2\dot{\bar{i}}_\alpha + k_3\bar{i}_\alpha + Y_\alpha\right] \\ +i_\beta\left[k_1\left(\frac{2}{1+(|\bar{i}_\beta|+1)^{-z\bar{i}_\beta}}\right)h(\bar{i}_\beta) + k_2\dot{\bar{i}}_\beta + k_3\bar{i}_\beta + Y_\beta\right] \end{pmatrix}\right\} \tag{17}$$

Given that the $h(x)$ function within the nonlinear term possesses boundedness and smoothness, by designing appropriate k_i control parameters to manage its nonlinear influence, it can be ensured that $\dot{V} \leq 0$, thus guaranteeing the global asymptotic stability of the system.

4. ROTOR POSITION EXTRACTION AND COMPENSATION

4.1. Traditional Phase-Locked Loop

In the high-performance control of permanent-magnet synchronous motors, the phase-locked loop achieves the precise adjustment of speed and torque through closed-loop feedback. It continuously compares the actual rotor position with the reference value and dynamically adjusts the output using the error signal, thereby suppressing speed fluctuations, enhancing the torque response, and ensuring the stable command tracking of the system. A block diagram of the conventional PLL structure is shown in Fig. 8.

In Fig. 8, $\hat{E}_\alpha$ and $\hat{E}_\beta$ represent the estimated values of the motor's back electromotive force on the α and β axes, respectively; k_p and k_i are the proportional and integral coefficients of the PI regulator; $\hat{\omega}_e$ and $\hat{\theta}_e$ are the estimated values of the motor's electrical angular velocity and rotor angle, respectively.

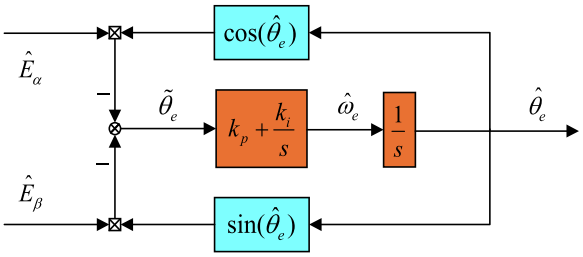

FIGURE 8. Traditional PLL block diagram.

The following relationship can be derived from the figure:

$$\tilde{\theta}_e = -\hat{e}_\alpha \cos\hat{\theta}_e - \hat{e}_\beta \sin\hat{\theta}_e = e_s\left(\sin\theta_e\cos\hat{\theta}_e - \cos\theta_e\sin\hat{\theta}_e\right)$$
$$= e_s \sin\left(\theta_e - \hat{\theta}_e\right) \tag{18}$$

When the rotor position error is small, after normalization using the above Equation, the rotor position error can be expressed as

$$\tilde{\theta}_e = \sin\left(\theta_e - \hat{\theta}_e\right) = \theta_e - \hat{\theta}_e \tag{19}$$

4.2. EDS-PLL

In the sensorless control of permanent magnet synchronous motors, the traditional phase-locked loop with a PI regulator, despite its simple structure and ease of implementation, often struggles to balance the dynamic response speed and steady-state accuracy during high-speed motor operation or during external disturbances. In particular, tracking the rotor position and speed is susceptible to chattering and noise interference. To further enhance the observation performance of the phase-locked loop under complex operating conditions, this study introduces a composite logarithmic sliding surface, as shown in Equation (20).

$$s_1 = \dot{\tilde{\theta}}_e + m\ln\left(n|\tilde{\theta}_e|^p + 1\right)\text{sign}(\tilde{\theta}_e) \tag{20}$$

where $\tilde{\theta}_e$ represents the rotor position error; $\dot{\tilde{\theta}}_e$ is the derivative of the variable; m, n, and p are constants.

Because the logarithmic function exhibits high sensitivity to minute errors, it enables a rapid and precise response to deviations, whereas the power-law function provides a smooth adjustment of the convergence process when errors are large, preventing overly aggressive system reactions. Integrating both functions into the sliding surface design of the phase-locked loop allows the system to approach the sliding surface swiftly when errors are small while maintaining smooth and stable regulation characteristics even under large error conditions. This significantly suppresses the chattering problem inherent in traditional sliding-mode designs and simultaneously enhances the robustness against parameter variations and disturbances.

To verify the convergence of the proposed sliding surface, assuming that the system converges to the sliding surface, that is, $s_1 = 0$ in Equation (20), the following can be derived:

$$\dot{\tilde{\theta}}_e = -m\ln\left(n|\tilde{\theta}_e|^p + 1\right)\text{sign}(\tilde{\theta}_e) \tag{21}$$

Thus, the Lyapunov function is selected as:

$$V = \frac{1}{2}\tilde{\theta}_e^2 \tag{22}$$

Taking its derivative yields:

$$\dot{V} = \tilde{\theta}_e \cdot \dot{\tilde{\theta}}_e = \tilde{\theta}_e\left[-m\ln\left(n|\tilde{\theta}_e|^p + 1\right)\right]\text{sign}(\tilde{\theta}_e)$$
$$= \tilde{\theta}_e \cdot \text{sign}(\tilde{\theta}_e) \cdot \left[-m\ln\left(n|\tilde{\theta}_e|^p + 1\right)\right] \tag{23}$$

Since $-m\ln(n|\tilde{\theta}_e|^p + 1) < 0$ and $\tilde{\theta}_e \cdot \text{sign}(\tilde{\theta}_e) > 0$, it can be concluded that $\dot{V} \le 0$. This indicates that Equation (20) can achieve finite-time stable convergence, and both its reaching process and stability satisfy the fundamental requirements for sliding surfaces in the sliding mode control theory.

The motor motion equation is shown in Equation (24):

$$\begin{cases} \dot{\theta}_e = \omega_e \\ \dot{\omega}_e = ai_q^* + z \\ \dot{z} = 0 \end{cases} \tag{24}$$

where z represents the lumped disturbance, a the angular acceleration, and i_q the reference current along the q axis. Based on the above equation, an extended state sliding-mode phase-locked loop is designed as follows:

$$\begin{cases} \dot{\hat{\theta}}_e = \hat{\omega}_e + \gamma_1 s_2 \\ \dot{\hat{\omega}}_e = ai_q^* + \hat{z} + \gamma_2 s_2 \\ \dot{\hat{z}} = \gamma_3 \text{sign}(\hat{\theta}_e) \end{cases} \tag{25}$$

where γ_1, γ_2, and γ_3 are the gain coefficients of the phase-locked loop, and $s_2 = m\ln(n|\hat{\theta}_e|^p + 1)\text{sign}(\hat{\theta}_e)$ represents the integral term. Since the controller includes an integral component, it can, on one hand, attenuate chattering phenomena and, on the other hand, eliminate steady-state error in the system, thereby enhancing the overall control quality.

To further enhance the tracking accuracy of the speed and rotor position, as well as to improve the system's robustness, the composite nonlinear transition function $h(x)$ proposed above was introduced to replace the switching function sign( ). By leveraging the piecewise characteristics of the nonlinear function, a sine function is employed in small-error regions for smooth processing to reduce high-frequency oscillations, whereas a logarithmic function is used in large-error regions to amplify the error effect and accelerate the convergence speed. This approach improves dynamic performance and disturbance rejection capability. Thus, Equation (25) can be rewritten as

$$\begin{cases} \dot{\hat{\theta}}_e = \hat{\omega}_e + \gamma_1 s_3 \\ \dot{\hat{\omega}}_e = ai_q^* + \hat{z} + \gamma_2 s_3 \\ \dot{\hat{z}} = \gamma_3 f(\hat{\theta}_e) \end{cases} \tag{26}$$

where $s_3 = m\ln(n|\hat{\theta}_e|^p + 1)f(\hat{\theta}_e)$.

From Equations (24) and (26), the error state equation is obtained as:

$$\begin{cases} \dot{\tilde{\theta}}_e = \tilde{\omega}_e - \gamma_1 s_\varepsilon \\ \dot{\tilde{\omega}}_e = \tilde{z} - \gamma_2 s_\varepsilon \\ \dot{\tilde{z}} = -\gamma_3 f(\tilde{\theta}_e) \end{cases} \tag{27}$$

where $s_\varepsilon = m\ln(n|\tilde{\theta}_e|^p + 1)f(\tilde{\theta}_e)$; $\tilde{\omega}_e$ represent the angular velocity estimation error, and $\tilde{z}$ denotes the lumped disturbance estimation error.

The fundamental principle of the EDS-PLL proposed in this study is illustrated in Fig. 9.

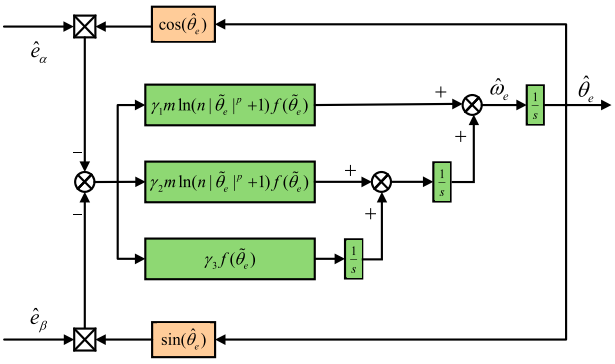

FIGURE 9. Block diagram of the EDS-PLL.

4.3. Compensation Mechanism

The closed-loop speed in this study uses the value filtered by a low-pass filter (LPF), whereas the speed in SMO is unfiltered. Consequently, there is an inevitable deviation between the estimated rotor position and the actual rotor position. This deviation, denoted as η_{error}, is given by

$$\eta_{error} = \int \hat{\omega}_p \mathrm{d}t - \int \hat{\omega}_e \mathrm{d}t \tag{28}$$

Additionally, to compensate for the rotor-position estimation errors caused by components such as LPF and PLL, the expression for the error quantity δ is defined as

$$\delta = -i_\alpha \sin\hat{\theta}_e + i_\beta \cos\hat{\theta}_e = \sqrt{i_\alpha^2 + i_\beta^2}\sin\left(\theta_e - \hat{\theta}_e\right) \tag{29}$$

From Equation (29), it can be seen that δ contains rotor position error information. The error compensation value, l, can be obtained by utilizing the closed-loop phase-tracking principle of the PLL.

Based on the above analysis, the rotor position error compensation can be composed of two parts: error compensation quantity l and deviation quantity η_{error}. The final rotor position can be expressed as:

$$\hat{\theta}_e = l + \eta_{error} + \hat{\theta}_{SMO} \tag{30}$$

where $\hat{\theta}_{SMO}$ represents the rotor position output from the phase-locked loop.

The fundamental principle of the compensated EDS-PLL proposed in this study is illustrated in Fig. 10.

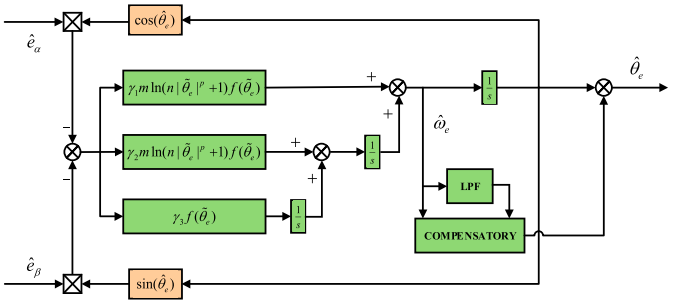

FIGURE 10. Block diagram of the compensated EDS-PLL.

4.4. Stability Proof

Select the Lyapunov function:

$$V = \frac{1}{2}\tilde{\theta}_e^2 \tag{31}$$

Substituting Equation (27) into Equation (31) and differentiating, the Lyapunov function can be expressed as:

$$\dot{V} = \tilde{\theta}_e \cdot \dot{\tilde{\theta}}_e = \tilde{\theta}_e\left(\tilde{\omega}_e - \gamma_1 s_\varepsilon\right) \tag{32}$$

Because s_ε and $\tilde{\theta}_e$ have the same sign, when $\gamma_1 > \tilde{\omega}_e / s_\varepsilon$ is satisfied, the following can be derived:

$$\dot{V} = \tilde{\theta}_e \cdot \dot{\tilde{\theta}}_e < 0 \tag{33}$$

Equation (33) ensures that the system reaches the sliding surface; however, it does not guarantee convergence to the sliding surface within a finite time. When the system converges to the sliding surface, the following is obtained:

$$\tilde{\omega}_e = \gamma_1 s_\varepsilon \tag{34}$$

Substituting Equation (34) into Equation (27), we obtain:

$$\begin{cases} \tilde{\omega}_e = \gamma_1 s_\varepsilon \\ \dot{\tilde{\omega}}_e = \tilde{z} - \gamma_2 s_\varepsilon \\ \dot{\tilde{z}} = -\gamma_3 f(\tilde{\theta}_e) \end{cases} \tag{35}$$

When the system reaches the vicinity of the sliding surface, the error equations for the angular velocity and lumped disturbance are given by Equation (35). When conditions $\gamma_1 > 0$, $\gamma_2 > 0$, and $\gamma_3 > 0$ are satisfied, it can be derived from Equation (35) that when $\tilde{\theta}_e > 0$, then $s_\varepsilon > 0$, $\tilde{\omega}_e > 0$, and $\dot{\tilde{z}} < 0$, which leads to the conclusion $\dot{\tilde{\omega}}_e < 0$, that is, $\dot{\tilde{\omega}}_e \cdot \tilde{\omega}_e < 0$, $\tilde{\theta}_e$ gradually tends to 0, and $\tilde{z}$ gradually tends to 0. When $\tilde{\theta}_e < 0$, then $s_\varepsilon < 0$, $\tilde{\omega}_e < 0$, and $\dot{\tilde{z}} > 0$, which leads to $\dot{\tilde{\omega}}_e > 0$, that is, $\dot{\tilde{\omega}}_e \cdot \tilde{\omega}_e < 0$; $\tilde{\theta}_e$ gradually tends to 0, and $\tilde{z}$ gradually tends to 0.

5. SIMULATION ANALYSIS

To validate the effectiveness of the combination of HAFSMO and EDS-PLL proposed in this study, three schemes are proposed for comparison: Scheme 1 is SMO-PLL; Scheme 2 is STASMO-NPLL [23]; and Scheme 3 is HAFSMO-EDS-PLL. Based on the system control block diagram shown in Fig. 11,

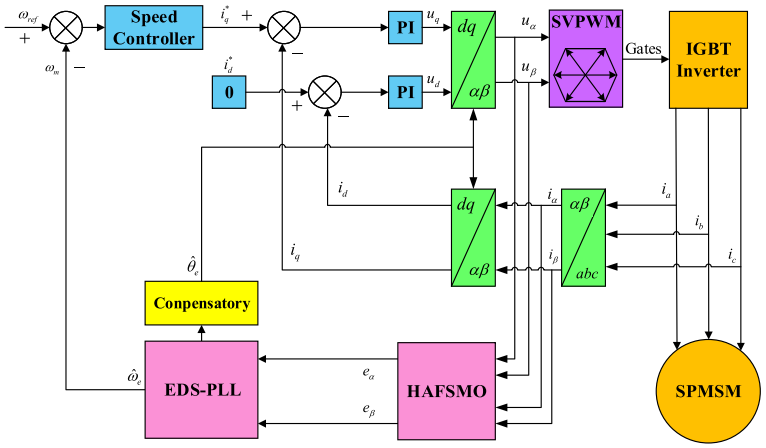

FIGURE 11. Block diagram of the PMSM system control.

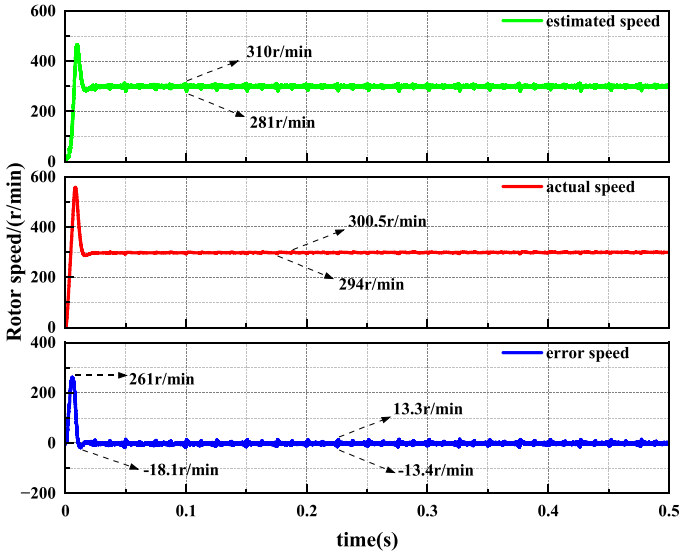

FIGURE 12. No-load speed waveform of SMO-PLL.

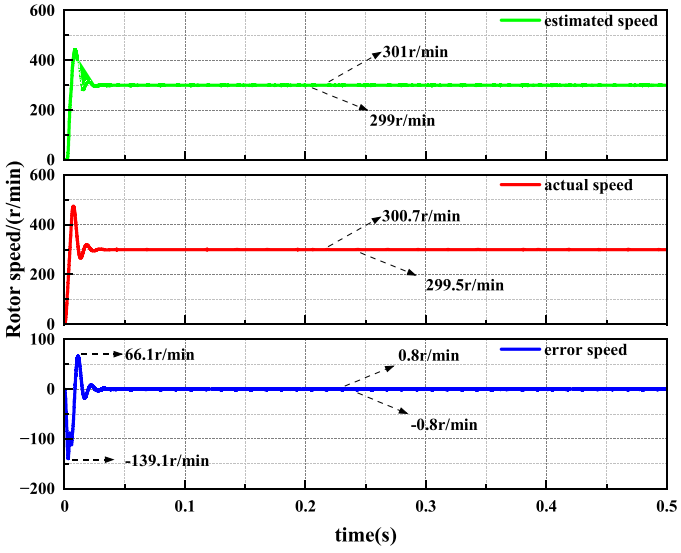

FIGURE 13. No-load speed waveform of STASMO-NPLL.

simulations were conducted using MATLAB/Simulink software. The current loop and speed loop employ conventional PI control with a DC bus voltage of 311 V and a sampling period of 10 μs.

5.1. No-Load Speed Analysis

To validate the speed control effectiveness of the different sliding mode observer schemes, a reference speed of 300 r/min was set. Figs. 12, 13, and 14 present the speed waveforms under three schemes: SMO-PLL, STASMO-NPLL, and HAFSMO-EDS-PLL, respectively. The comparative simulation results are as follows. For SMO-PLL, the chattering in the estimated speed versus the actual speed is 29 r/min and 6.5 r/min, respectively, with a steady-state speed error chattering of 26.7 r/min and an initial oscillation range of 261 r/min to −18.1 r/min. For STASMO-NPLL, the chattering in the estimated speed versus the actual speed is 2 r/min and 1.2 r/min, respectively, with a steady-state speed error chattering of 1.6 r/min and an initial oscillation range of 66.1 r/min to −139.1 r/min. For HAFSMO-EDS-PLL, the chattering in the estimated speed versus the actual speed is 0.4 r/min and 0.3 r/min, respectively, with a steady-state speed error chattering of 0.56 r/min and an initial oscillation range of 48 r/min to −108 r/min. The simulation results indicate that the HAFSMO-EDS-PLL demonstrates optimal performance in terms of chattering in both estimated and actual speeds, steady-state error chattering, and initial oscillation amplitude, which effectively validates the comprehensive advantages of this method in suppressing chattering, reducing steady-state error, and enhancing disturbance rejection capability.

5.2. Load Speed Analysis

To evaluate the disturbance rejection performance of different control strategies under dynamic load conditions, a reference speed of 300 r/min was set, with a sudden load increase of 10 N·m applied at 0.2 s and an equal load decrease at 0.4 s. The speed waveforms under the three schemes, SMO-PLL, STASMO-NPLL, and HAFSMO-EDS-PLL are presented

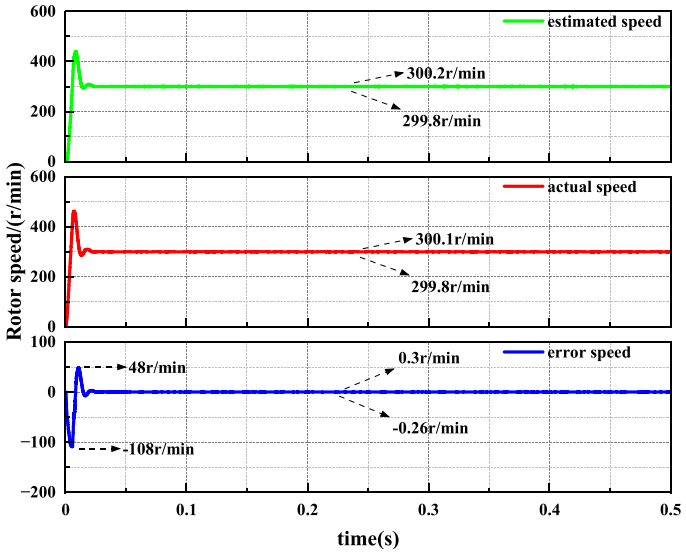

FIGURE 14. No-load speed waveform of HAFSMO-EDS-PLL.

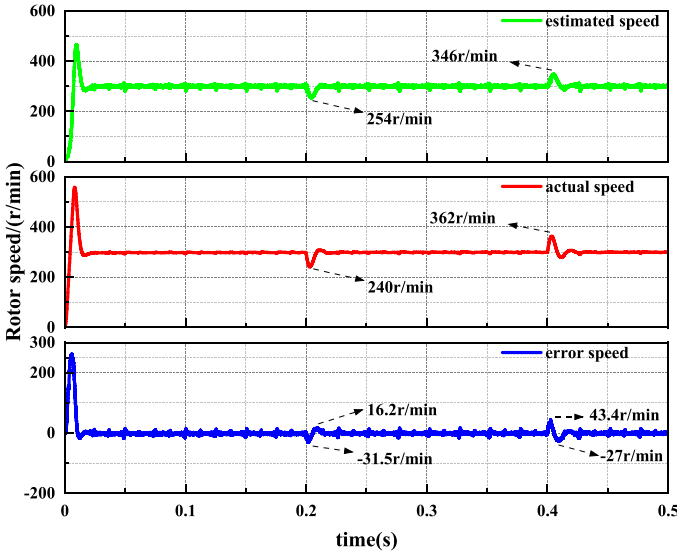

FIGURE 15. SMO-PLL load speed waveform diagram.

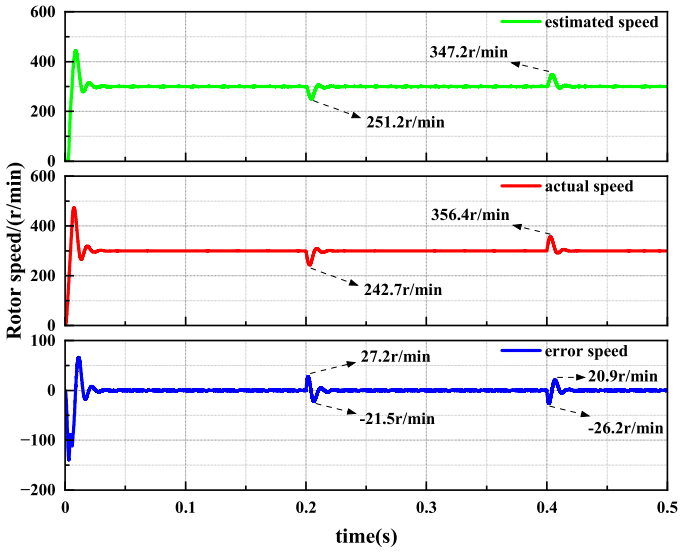

FIGURE 16. STASMO-NPLL load speed waveform diagram.

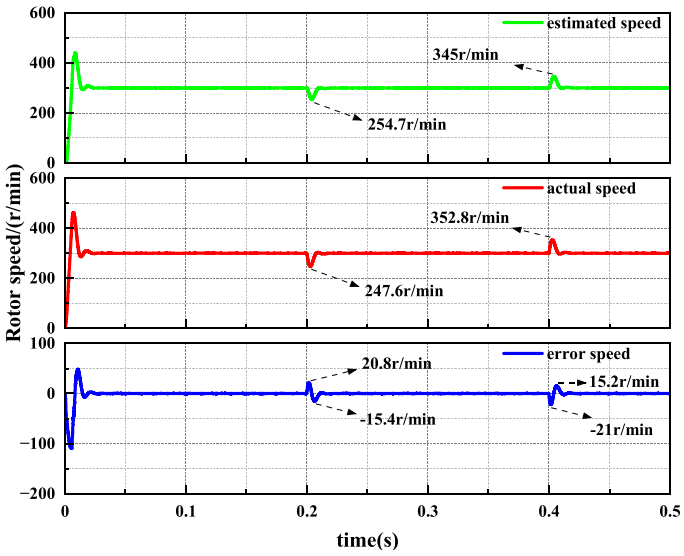

FIGURE 17. HAFSMO-EDS-PLL speed waveform diagram.

in Figs. 15, 16, and 17, respectively. The comparative simulation results are as follows: For SMO-PLL, upon load increase, the estimated and actual speeds decrease by 46 r/min and 60 r/min, respectively, with the speed error varying between 31.5 r/min and 16.2 r/min; upon load decrease, the estimated and actual speeds increase by 46 r/min and 62 r/min, respectively, with the speed error ranging from 27 r/min to 43.4 r/min. For STASMO-NPLL, upon load increase, the estimated and actual speeds decrease by 48.8 r/min and 57.3 r/min, respectively, with the speed error varying between 21.5 r/min and 27.2 r/min; upon load decrease, the estimated and actual speeds increase by 47.2 r/min and 56.4 r/min, respectively, with the speed error ranging from 26.2 r/min to 20.9 r/min. For HAFSMO-EDS-PLL, upon load increase, the estimated and actual speeds decrease by 45.3 r/min and 52.4 r/min, respectively, with the speed error varying between 15.4 r/min and 20.8 r/min; upon load decrease, the estimated and actual speeds increase by 45 r/min and 52.8 r/min, respectively, with the speed error ranging from 21 r/min to 15.2 r/min. The simulation results indicate that the HAFSMO-EDS-PLL exhibits the smallest magnitude of speed drop and rise, along with the narrowest fluctuation range in the speed error during sudden load changes. This demonstrates its strong load-carrying capability, superior robustness, and dynamic regulation performance, thereby confirming that it provides the best overall control effectiveness among the three schemes.

5.3. Rotor Position Analysis

In the rotor position analysis of this section, the simulation conditions remain consistent with Section 5.1 (no-load speed analysis): the motor reference speed is set to 300 r/min under a no-load operating condition. Figs. 18–20 present the observed rotor position waveforms and their corresponding errors for the three schemes SMO-PLL, STASMO-NPLL, and HAFSMO-

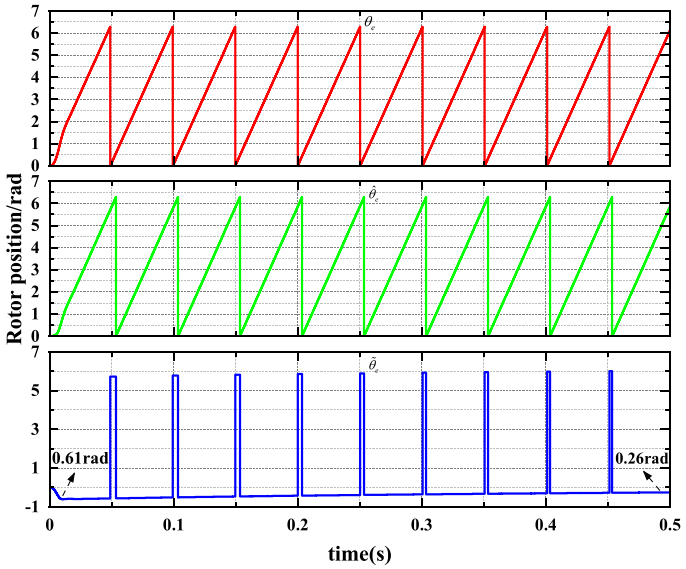

FIGURE 18. SMO-PLL rotor position waveform diagram.

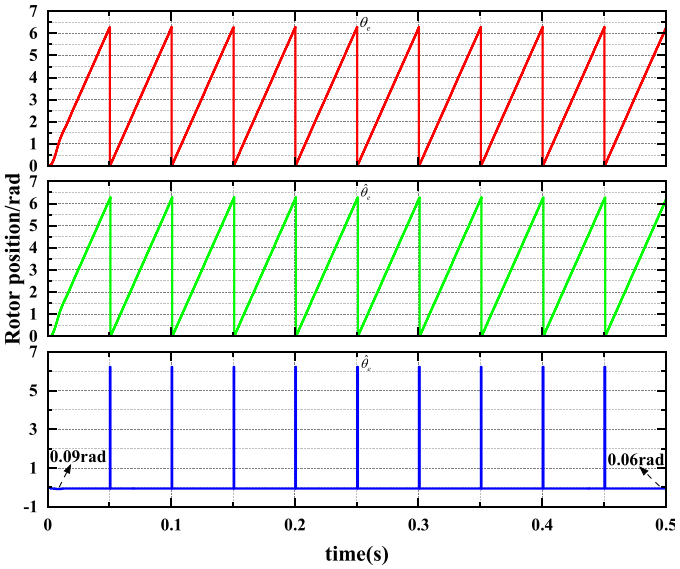

FIGURE 19. STASMO-NPLL rotor position waveform diagram.

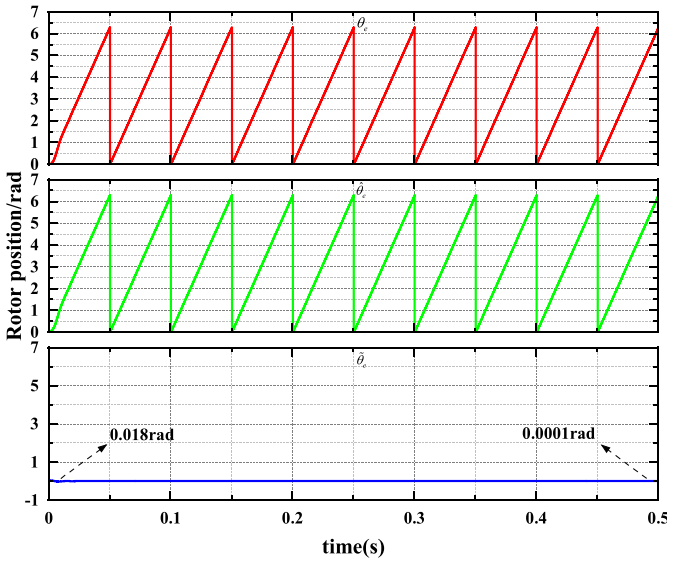

FIGURE 20. HAFSMO-EDS-PLL rotor position waveform diagram.

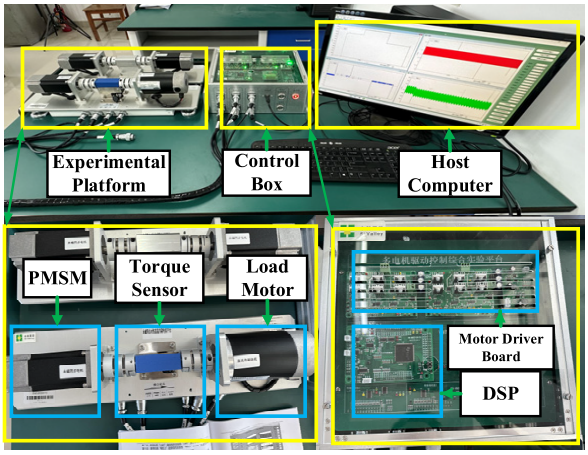

FIGURE 21. Experimental platform for motor drive control system.

EDS-PLL under this operating condition. A comparison of the rotor position observation accuracy for each scheme is as follows: For SMO-PLL, the steady-state rotor position error is approximately 0.43 rad; the error is about 0.61 rad in the initial stage and decreases to 0.26 rad by the end of the simulation. For STASMO-NPLL, the steady-state rotor position error is approximately 0.063 rad; the error is about 0.09 rad in the initial stage and around 0.06 rad at the end. For HAFSMO-EDS-PLL, the steady-state rotor position error is only 0.0002 rad; the error is approximately 0.018 rad in the initial stage, and further is reduced to 0.0001 rad by the end. The simulation results demonstrate that the HAFSMO-EDS-PLL exhibits significantly superior accuracy in rotor position estimation. Both its steady-state error and the error magnitude during the dynamic process are markedly lower than those of the other two schemes, validating the effectiveness of the HAFSMO-EDS-PLL in enhancing system control precision and overall performance.

6. EXPERIMENTAL ANALYSIS

To validate the feasibility and effectiveness of the proposed HAFSMO-EDS-PLL method and to compare its performance with that of SMO-PLL and STASMO-NPLL, an experimental platform for a motor drive control system with TMS320F28335 at its core was established. The structure of the platform is illustrated in Fig. 21. The experimental setup primarily consisted of an upper computer, permanent magnet synchronous motor, torque sensor, power drive module, and DC brushed motor. The nameplate parameters of the PMSM are as follows: rated power 400 W, rated speed 3000 r/min, stator resistance 0.25 Ω, inductance 0.5 mH, moment of inertia 0.00003 kg·m^2, back-EMF coefficient 6.8 V/(m/s), pole pairs 4, rated voltage 48 V, rated current 12.5 A. The sampling frequency of the system was set to 10 kHz. The load torque was simulated using a direct-current (DC) brushed motor. Simultaneously, a 2500-line incremental encoder was installed on the motor shaft end to detect the actual position and speed of the PMSM rotor and to provide feedback for calculating the estimation errors.

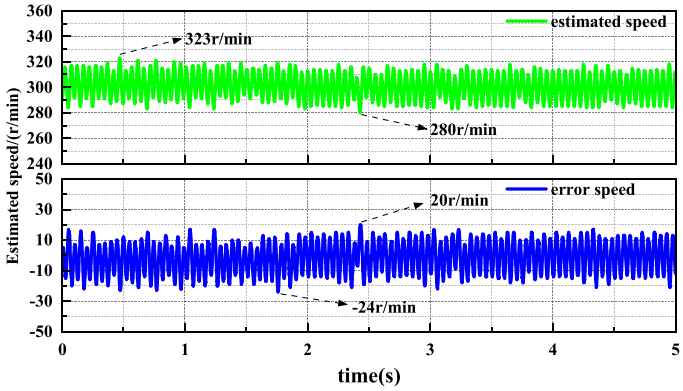

FIGURE 22. No-load experimental speed waveform of SMO-PLL.

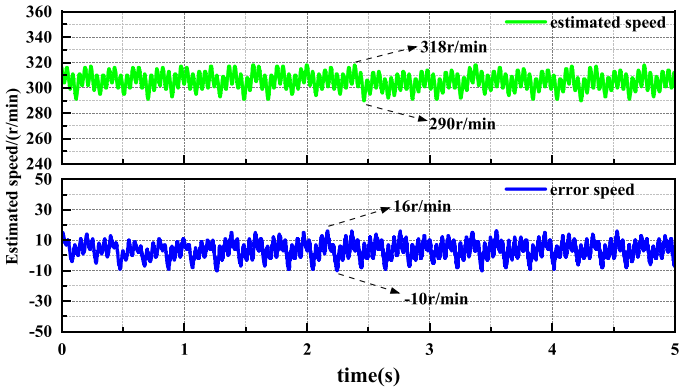

FIGURE 23. No-load experimental speed waveform of STASMO-NPLL.

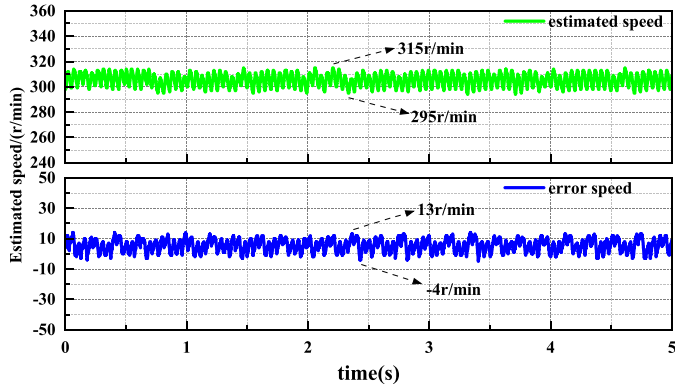

FIGURE 24. No-load experimental speed waveform of HAFSMO-EDS-PLL.

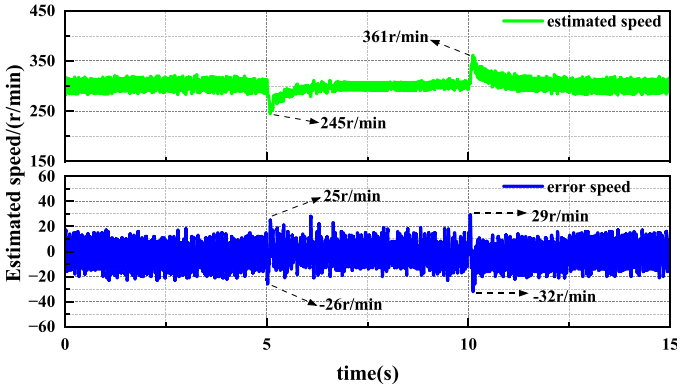

FIGURE 25. Load experimental speed waveform of SMO-PLL.

Regarding the computational complexity issue, this study conducted an analysis based on the hardware experimental platform DSP TMS320F28335 (main frequency $f_{CPU} = 150\,\text{MHz}$). In MATLAB/Simulink, the simulation duration was set to 0.5 s, and the Auto (ode45) solver was selected for simulation.

According to the measurements, the total number of simulation steps for the HAFSMO-EDS-PLL algorithm is $N_{step} = 142957$, while that for the comparative algorithm SMO-PLL is $N_{step} = 50297$. Based on the DSP machine cycle calculation formula $t_{step} = 1/f_{CPU}$, the single instruction cycle is obtained as 6.67×10^{-9} s. Further calculations yield: the total execution time of HAFSMO-EDS-PLL on the DSP is $142957 \times 6.67 \times 10^{-9} = 9.5352319 \times 10^{-4}$ s, and that of SMO-PLL is $50297 \times 6.67 \times 10^{-9} = 3.3548099 \times 10^{-4}$ s.

The results show that the number of simulation steps for HAFSMO-EDS-PLL is 2.84 times that of SMO-PLL, and its execution time on the DSP is correspondingly 2.84 times that of the latter. However, thanks to the powerful real-time processing capability of the TMS320F28335, the actual execution times of both algorithms are on the same order of magnitude (seconds), fully meeting the real-time requirements of the system. Moreover, the performance improvements brought by HAFSMO-EDS-PLL in terms of observation accuracy, chattering suppression, and dynamic response significantly outweigh the increased computational overhead, verifying the effectiveness and advantages of this algorithm in engineering practice.

6.1. Experimental Analysis of No-Load Speed

With the motor speed set to 300 r/min, Figs. 22, 23, and 24 present the estimated speed and speed error waveforms under no-load conditions for three control schemes: SMO-PLL, STASMO-NPLL, and HAFSMO-EDS-PLL, respectively. The experimental results show that the chattering range of the estimated speed for the SMO-PLL is approximately 280–323 r/min, with a speed error of 44 r/min. For STASMO-NPLL, the chattering range is approximately 290–318 r/min, with a speed error of 26 r/min. In contrast, for the HAFSMO-EDS-PLL, the chattering range is approximately 295–315 r/min, and the speed error is only 17 r/min. The comparison indicates that the HAFSMO-EDS-PLL method not only exhibits the smallest chattering amplitude but also significantly reduces speed error. This demonstrates the superior performance of this method in suppressing chattering, enhancing the system stability, and improving the speed accuracy.

6.2. Load Experiment Speed Analysis

Under the operating condition of a motor speed of 300 r/min, a sudden load increase was applied at the 5th second and a

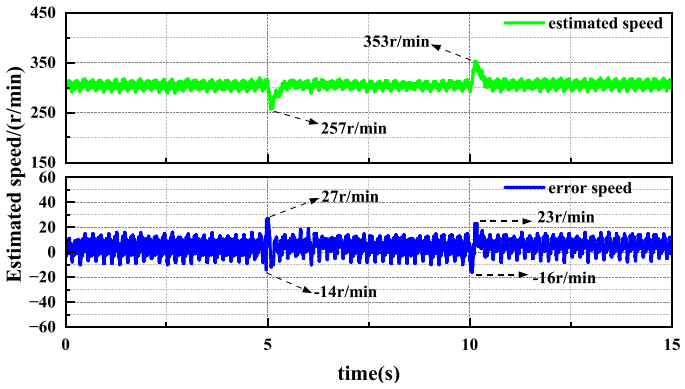

FIGURE 26. Load experimental speed waveform of STASMO-NPLL.

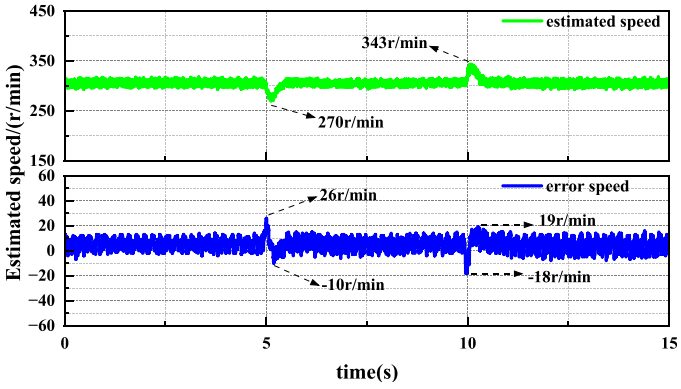

FIGURE 27. Load experimental speed waveform of HAFSMO-EDS-PLL.

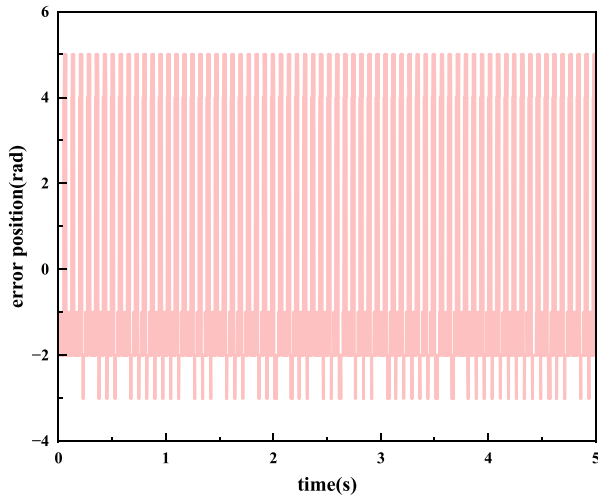

FIGURE 28. Experimental results of rotor position error for SMO-PLL.

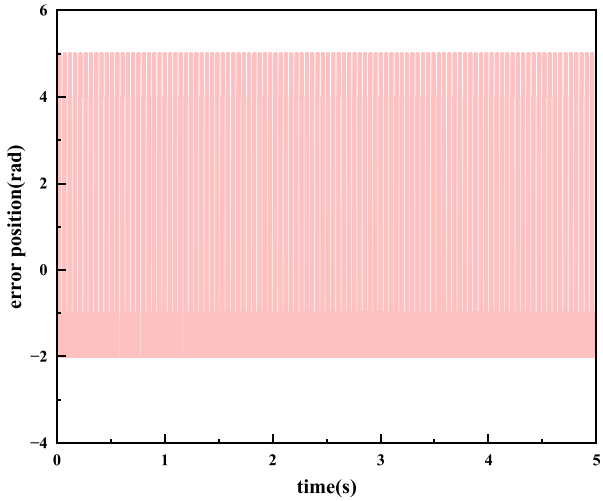

FIGURE 29. Experimental results of rotor position error for STASMO-NPLL.

sudden load decrease at the 10th second to validate the dynamic response capability of the control system. Figs. 25, 26, and 27 show the estimated speed and speed error waveforms of the three methods-SMO-PLL, STASMO-NPLL, and HAFSMO-EDS-PLL under sudden load changes. From the figures, it can be observed that during the sudden load increase, the speed of the SMO-PLL drops by approximately 55 r/min, with a speed error fluctuation range of −26 r/min to 25 r/min; the speed of STASMO-NPLL drops by approximately 43 r/min, with an error range of −14 r/min to 27 r/min, whereas the speed of the HAFSMO-EDS-PLL drops only by 30 r/min, with an error range of −10 r/min to 26 r/min. During the sudden load decrease, the speed of the SMO-PLL increases by approximately 61 r/min, with an error range of −32 r/min to 29 r/min; the speed of STASMO-NPLL increases by approximately 53 r/min, with an error range of −16 r/min to 23 r/min; and the speed of the HAFSMO-EDS-PLL increases by approximately 43 r/min, with an error range of −18 r/min to 19 r/min. The comparison indicates that the HAFSMO-EDS-PLL exhibits the smallest amplitude of speed fluctuation during sudden load changes, demonstrating that this method exhibits stronger load adaptability, superior dynamic performance, and higher control precision.

6.3. Experimental Analysis of Rotor Position Error

To compare the rotor position estimation accuracy of the different methods, Figs. 28, 29, and 30 present the rotor position error waveforms for the three schemes: SMO-PLL, STASMO-NPLL, and HAFSMO-EDS-PLL, respectively. The experimental results show that the rotor position error of SMO-PLL is approximately 2 rad, and because of the chattering effects, it can fluctuate up to 3 rad during dynamic processes. STASMO-NPLL stabilizes the error at approximately 2 rad, whereas HAFSMO-EDS-PLL further reduces the error to approximately 1 rad, demonstrating the best performance. The experimental findings indicate that the SMO-PLL suffers from relatively large position errors and insufficient stability owing to the inherent chattering issue caused by sliding-mode switching. By combining STASMO with NPLL, STASMO-NPLL effectively suppresses chattering and enhances disturbance rejection capability. The HAFSMO-EDS-PLL further improves the dynamic response and steady-state accuracy by introducing EDS-PLL on the basis of HAFSMO, thereby achieving the smallest rotor position error.

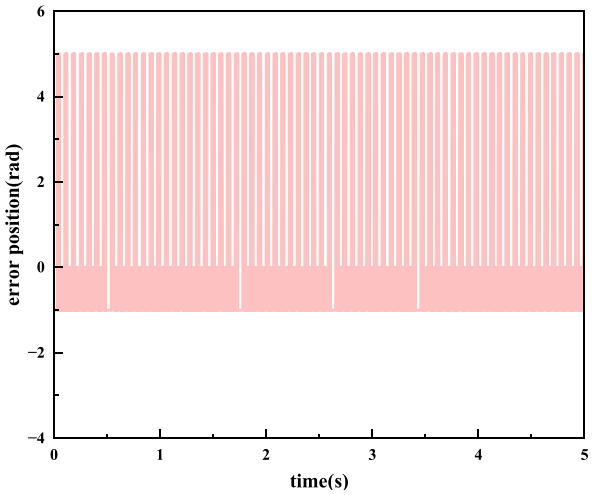

FIGURE 30. Experimental results of rotor position error for HAFSMO-EDS-PLL.

7. CONCLUSION

This paper proposes a composite control strategy that combines a fuzzy adaptive higher-order sliding mode observer with a composite logarithmic sliding-mode phase-locked loop. The main outcomes were as follows:

First, an adaptive higher-order sliding-mode observer (HAFSMO) was designed to replace the traditional sliding-mode observer. By introducing an exponential saturation smoothing function, adaptive gains, a compensation term, and increasing the system order, the dynamic response and disturbance rejection capabilities of the sliding-mode observer are significantly enhanced. Furthermore, fuzzy control was employed to dynamically adjust the boundary layer thickness, effectively suppressing the high-frequency chattering problem caused by discontinuous switching control.

Second, a composite logarithmic sliding-mode phase-locked loop (EDS-PLL) was proposed to replace the traditional PLL structure. This method integrates the exponential saturation smoothing function with a logarithmic sliding surface and incorporates a position compensation mechanism to reduce the rotor position error. It not only improves the estimation performance of the rotor position and speed, but also maintains an accurate observation performance under various operating conditions.

Finally, the performance of the SMO-PLL, STASMO-NPLL, and the proposed HAFSMO-EDS-PLL method are compared under various conditions, such as no-load and sudden load changes, using both a MATLAB/Simulink simulation platform and an experimental motor drive control platform based on TMS320F28335. The results demonstrate that the proposed method exhibits significant advantages in terms of chattering suppression, estimation accuracy, and dynamic response, thus fully validating its effectiveness and advanced nature.

ACKNOWLEDGEMENT

This work was supported by the Research Foundation of Jiangsu Engineering Research Center for Bionics Control Technology and Equipment under No. FSKZ202503.

REFERENCES

[1] Sreenivasu, S. V. N., T. S. Kumar, O. B. Hussain, A. R. Yeruva, S. R. Kabat, and A. Chaturvedi, "Cloud based electric vehicle's temperature monitoring system using IOT," *Cybernetics and Systems*, Vol. 56, No. 6, 768–783, 2025.

[2] Peng, Y., F. Chen, F. Chen, C. Wu, Q. Wang, Z. He, and S. Lu, "Energy-efficient train control: A comparative study based on permanent magnet synchronous motor and induction motor," *IEEE Transactions on Vehicular Technology*, Vol. 73, No. 11, 16 148–16 159, 2024.

[3] Wang, S., J. Su, G. Lu, and G. Yang, "Decoupling control for aviation dual-redundancy permanent magnet synchronous motor with 0° phase shift," *IEEE Transactions on Energy Conversion*, Vol. 38, No. 4, 2929–2937, 2023.

[4] Jin, X., L. Zhou, T. Lang, and Y. Jiang, "Low-voltage water pump system based on permanent magnet synchronous motor," *Electronics*, Vol. 13, No. 18, 3674, 2024.

[5] Ran, Y., M. Qiao, L. Sun, and Y. Xia, "Review of position sensorless control technology for permanent magnet synchronous motors," *Energies*, Vol. 18, No. 9, 2302, 2025.

[6] Zhang, H., W. Liu, Z. Chen, and N. Jiao, "An overall system delay compensation method for IPMSM sensorless drives in rail transit applications," *IEEE Transactions on Power Electronics*, Vol. 36, No. 2, 1316–1329, 2021.

[7] Sun, X., Y. Zhang, X. Tian, J. Cao, and J. Zhu, "Speed sensorless control for IPMSMs using a modified MRAS with gray wolf optimization algorithm," *IEEE Transactions on Transportation Electrification*, Vol. 8, No. 1, 1326–1337, 2022.

[8] Ye, S. and X. Yao, "An enhanced SMO-based permanent-magnet synchronous machine sensorless drive scheme with current measurement error compensation," *IEEE Journal of Emerging and Selected Topics in Power Electronics*, Vol. 9, No. 4, 4407–4419, 2021.

[9] Niu, H., L. Liu, D. Jin, and S. Liu, "High-tracking-precision sensorless control of PMSM system based on fractional order model reference adaptation," *Fractal and Fractional*, Vol. 7, No. 1, 21, 2023.

[10] Kong, X. and Q. Yuan, "Disturbance-rejection control of permanent magnet synchronous motors using robust adaptive extended Kalman filter," *IEICE Electronics Express*, Vol. 22, No. 18, 20250397, 2025.

[11] Yang, H., J.-W. Tang, and Y.-R. Chien, "Application of new sliding mode control in vector control of PMSM," *IEICE Electronics Express*, Vol. 19, No. 13, 20220156, 2022.

[12] Wang, Y., J. Wu, Z. Guo, C. Xie, J. Liu, and X. Jin, "Flux-weakening fuzzy adaptive ST-SMO sensorless control algorithm for PMSM in EV," *The Journal of Supercomputing*, Vol. 78, No. 8, 10 930–10 949, 2022.

[13] Ren, N., L. Fan, and Z. Zhang, "Sensorless PMSM control with sliding mode observer based on sigmoid function," *Journal of Electrical Engineering & Technology*, Vol. 16, No. 2, 933–939, 2021.

[14] Wang, D. and X. Liu, "Sensorless control of PMSM with improved adaptive super-twisting sliding mode observer and IST-QSG," *IEEE Transactions on Transportation Electrification*, Vol. 11, No. 1, 721–731, 2025.

[15] Song, C., W. Hu, J. Zhang, C. Zhao, and X. Sun, "A gain adaptive high-order terminal sliding mode observer under SPMSM sensorless control," *IEEE Transactions on Power Electronics*, Vol. 40, No. 5, 6555–6565, 2025.

[16] Gong, C., Y. Hu, J. Gao, Y. Wang, and L. Yan, "An improved delay-suppressed sliding-mode observer for sensorless vector-

controlled PMSM," *IEEE Transactions on Industrial Electronics*, Vol. 67, No. 7, 5913–5923, 2020.

[17] Yu, M. and Z. Wang, "Sensorless control of permanent magnet synchronous motors based on composite nonlinear functions and ESO-PLLs," *Electrical Engineering*, Vol. 108, No. 1, 46, 2026.

[18] Yao, G., X. Wang, Z. Wang, and Y. Xiao, "Senseless control of permanent magnet synchronous motors based on new fuzzy adaptive sliding mode observer," *Electronics*, Vol. 12, No. 15, 3266, 2023.

[19] Liu, X., Z. Wang, W. Wang, Y. Lv, B. Yuan, S. Wang, W. Li, Q. Li, Q. Zhang, and Q. Chen, "SMO-based sensorless control of a permanent magnet synchronous motor," *Frontiers in Energy Research*, Vol. 10, 839329, 2022.

[20] Wang, D., B. Li, and Y. Zhao, "An adaptive SMO approach for low-chattering sensorless control of PMSM," *IEEE Transactions on Power Electronics*, Vol. 40, No. 10, 15 329–15 338, 2025.

[21] Li, Y. and X. Liu, "Sensorless control of permanent magnet synchronous motor based on high-order sliding mode observer and improved PLL," *Journal of Electrical Engineering*, Vol. 18, No. 4, 96–105, 2023.

[22] Li, H., P. Zhi, H. Wei, Y. Zhang, and W. Zhu, "Research on sensorless control for permanent magnet synchronous motor based on ESO-PLL," in *2025 44th Chinese Control Conference (CCC)*, Chongqing, China, Jul. 2025.

[23] Zou, X., H. Ding, and J. Li, "Sensorless control strategy of permanent magnet synchronous motor based on adaptive super-twisting algorithm sliding mode observer," *Journal of Control, Automation and Electrical Systems*, Vol. 35, No. 1, 163–179, 2024.